High pinning performance of YBa2Cu3O7−x films added with Y2O3 nanoparticulate defects

Paolo Mele1, Roger Guzman2, Jaume Gazquez2, Teresa Puig2, Xavier Obradors2, Shrikant Saini1, Yutaka Yoshida3, Masashi Mukaida4, Ataru Ichinose5, Kaname Matsumoto6 and Malik Idries Adam7

1 Institute for Sustainable Sciences and Development, Hiroshima University, 1-3-1 Kagamiyama, Higashi-Hiroshima 739-8530, Japan

2 Institut de Ciencia de Materials de Barcelona, ICMAB-CSIC, Campus de la UAB, 08193 Bellaterra, Catalonia, Spain

3 Department of Electrical Engineering and Computer Science, Nagoya University, Furo-cho, Chikikusa-ku, Nagoya 464-8603, Japan

4 Department of Materials Science and Engineering, Kyushu University, 744 Motooka, Nishi-ku, Fukuoka 812-8581, Japan

5 Electric Power Engineering Research Laboratory, Central Research Institute of Electric Power Industry, 2-6-1 Nagasaka, Yokosuka, Kanazawa 240-0196, Japan

6 Department of Materials Science and Engineering, Kyushu Institute of Technology, 1-1 Sensui-cho, Tobata-ku, Kitakyushu 804-8550, Japan

7 Department of Mechanical Engineering, University Tenaga Nasional, UniTen, 43000 Kajang, Selangor, Malaysia

Abstract

We report the epitaxial growth and superconducting properties of Y2O3-added YBa2Cu3Ox (YBCO) films grown on SrTiO3-buffered MgO substrates by pulsed-laser deposition using surface-modified YBCO targets. Areas of Y2O3 sectors on the YBCO target were increased to 5.44% and 9.22% of the total YBCO pellet in order to find a correlation between the Y2O3 content, morphology, and the pinning properties of YBCO+Y2O3 mixed films. The maximum global pinning forces, FP, at 77 K were 14.3 GN m−3 and 1.15 GN m−3 for the Y2O3 5.44A% and 9.22A%, respectively. The 5.44A% Y2O3-added sample presents a very high value of pinning force at 77 K, approaching the value obtained in YBCO films with added BaZrO3 nanorods, but with less depression in the superconducting critical temperature, Tc. In accordance with scanning transmission electron microscopy (STEM) observations, both films

present nanoparticulate Y2O3 dispersed in a YBCO matrix where Y2Ba4Cu8O16 (Y248) intergrowths were also observed. Consistent with the strong pinning theory, the size and distribution of randomly dispersed Y2O3 particles are optimal for the flux pinning of a 5.44A% Y2O3-YBCO film, while in the case of a 9.22A% film, the YBCO matrix is degraded by jam-packed Y248 intergrowth, which leads to a comparatively poor pinning performance. We further used the single-vortex dynamics model to account for vortex pinning in the samples. The 5.44A% Y2O3-YBCO film result shows good agreement with the model fit up to 4 T of the applied magnetic field.

1. Introduction

The incorporation of artificial pinning centers (APCs) into thestructure of high-temperature superconducting epitaxial films has recently become a prerequisite for achieving drastic improvement in the critical current density (Jc) and the global pinning force (FP) under a varying magnetic field, B [1–3]. Several nanoengineering techniques have recently been developed to address the insertion and control of APCs, and the transport performances of YBa2Cu3Ox (YBCO) and REBa2Cu3Ox, (RE = Nd, Sm, Eu, Gd, etc) films were dramatically enhanced by the incorporation of nanosized dopants [4–24]. However, these numerous reports have recently focused on the effect of the one–dimensional (1D) nanorod APCs as a secondary phase in YBCO films prepared by the pulsed-laser deposition (PLD) technique [7–15]. Amid this activity, several approaches were adopted, which can be exemplified in the following points: (i) decoration of the substrate surface by Y2O3 nanoislands, the result of which is to induce extended linear defects, such as dislocations, into epitaxially grown YBCO films [7]; (ii) ablation of a 'mixed target', which comprises a mixture of standard YBCO and a second phase as an impurity from a BaZrO3, YSZ, BaSnO3, or BaHfO3 compound [8–13]; (iii) ablation of a 'pie-shaped' [14] or 'surface-modified' [15] target, where an inserted slice or attached piece of the second phase can be ablated in a periodic fashion. The aim of this particular technique was to produce finely distributed nanorods throughout the entire film thickness. In the aforementioned examples, APCs act as caxis-correlated defects, yielding an enhanced in-field pinning performance together with a strong anisotropy of the angular dependence Jc (with a maximum for the B//c axis), which is a critical parameter for practical applications. For instance, in winding a superconducting magnet, the superconducting tape has to be bent into a curved shape. The efficiency of APCs across the coiled conductor must be preserved, regardless of the mutual orientation of the tape and the externally applied

magnetic field. The most challenging issue here is: what if one must have an isotropic pinning force of a 1D APC-doped conductor placed along a direction that is not parallel to the applied magnetic field? Therefore, considerable effort has been put into the preparation of superconducting thin films that incorporate three-dimensional (3D) APCs.

So far, several reports on 3D APCs have contributed to the emerging literature of YBCO-APCs [16–24]. By means of the PLD method, two main approaches were generally adopted for sample preparation. The first one is the periodic switching of two targets, where the main YBCO target and the dopant target were meant to yield finely tuned multilayers of a second phase, intertwined with a superconducting phase, into the film [16, 17]. The second approach uses the ablation of a surface-modified target, as reported in [18]. 3D APCs were also incorporated in trifluoroacetate-metal organic deposition using the all-chemical-routes approach, metal organic chemical vapor deposition, and gas phase condensation processes [19–24]. In contrast with the 1D APCs, the 3D APCs are mainly incorporated into superconductor films in the form of randomly dispersed nanoparticles. In our previous report [18], we fabricated high-quality YBCO films doped with low-concentration Y_2O_3 nanoparticles. The area of a tiny Y_2O_3 sector placed on top of the surface-modified YBCO target was only 2.51A% of the total target area. The film from the YBCO +Y_2O_3 2.51A% target produced a maximum global pinning force of F_P = 7.78 GN m−3 (77 K, 3 T). This amount of pinning force is equal to half the value obtained in a YBCO film with added $BaZrO_3$ nanorods [11], but without much depressing of the superconducting critical temperature, T_c. Up to this point, it is worth contemplating a few pressing questions. Is Y_2O_3 2.51A% the optimal amount of Y_2O_3 doping? Is it possible to control the size and distribution of 3D APCs inside the films by varying the area of the Y_2O_3 sector? Can one tune the pinning force using these particular types of dopants? This paper aims to contribute to the answers of these questions. Hence, an attempt has been made to find a possible correlation between morphology and the pinning properties of YBCO films incorporating higher amounts of Y_2O_3 3D APCs.

2. Experimental setup

A Lambda Physik KrF excimer laser (λ = 248 nm) was used to fabricate the YBCO thin films and their nanocomposite Y_2O_3 by the PLD technique on MgO (100) (Furuuchi, Tokyo, Japan), a single crystal that supported an $SrTiO_3$ (STO) buffer layer. STO-buffered MgO was selected to enhance Jc(B), as reported, for example, in [25]. An STO target was ablated to form the STO buffer layer on MgO (100) substrates. The details of the STO buffer development were reported separately [26]. A substrate temperature of 800 °C and an oxygen partial pressure of

200 mTorr were maintained during deposition of the YBCO films. A repetition rate of 5 Hz and a laser energy of 340 mJ per pulse were used while substrate-totarget separation was kept at a distance of 60 mm from the ablated target. At the end of the deposition, the films were cooled down to room temperature within an hour under an oxygen pressure of 500 Torr. For the deposition of a standard YBCO thin film, a pristine YBCO target was ablated with 6000 laser pulses. For YBCO +Y_2O_3 nanocomposite films, in a previous work [18], the surface of the same, standard YBCO target was modified by inserting a triangle-shaped volume of a Y_2O_3 sector with a 2.51% relative area into it. This sector was cut from 0.5 mm-thick polycrystalline Y_2O_3 substrate and attached to the YBCO target with a silver paste. Two additional sectors, each of which has an area of 5.44%, and 9.22% of the whole surface of the YBCO target were similarly used to incorporate the Y_2O_3 nanoparticulate into the film. The thickness of the standard and doped thin films varied between 290 and 300 nm. Overall, the films described in this work were prepared in the same experimental conditions as the YBCO+ 2.51A% Y_2O_3 film reported in [18], so a comparison of the results of both experiments can be fairly drawn. The crystal phases and the orientation of the YBCO +Y_2O_3 films were determined by θ–2θ x-ray diffraction and x-ray rocking curves with CuKα radiation. Cross sections of the films were analyzed by transmission electronmicroscopy (TEM) and aberration-corrected scanning transmission electron microscopy (STEM). Bright-field TEM experiments were carried out using a JEOL 2010F field emission gun microscope. High-angle annular dark-field scanning transmission electron microscopy (HAADF-STEM) microstructural analyses were performed in a Nion Ultra STEM operated at 100 kV and equipped with a Nion aberration corrector. Cross-sectional specimens were obtained by cutting the film along the (100) plane of the MgO substrate and then gluing the slices face on, joining the YBCO surfaces. These TEM specimens were thinned out by mechanical grinding, polishing, and dimpling. This process is followed by Ar-ion milling.

The critical current density (Jc) values of all samples were measured by the four-probe method using the physical property measurement system (Quantum Design) after patterning the microbridge shape with a strip 100 μm wide and 1 mm long by photolithography. To obtain good contacts, Au pads were deposited on thin films by RF sputtering. The Jc values were evaluated from the transport properties with the criterion of the electric field, E=1 μV cm−1. The current was always applied perpendicular to magnetic field B. The relationships between Jc and magnetic field B when the field was applied parallel to the c-axis of the film (B//c) were obtained at 77 K in the field range of 0–9 T. The angular dependence of Jc(θ), where θ is the angle between the applied magnetic field and the c-axis of the film, was also measured at 77 K and 1, 3, and 5 T using the same voltage criterion. Resistivity of the samples was measured

between 60 and 300 K in the absence of an external magnetic field to obtain the critical temperature, Tc.

3. Results and discussion

The θ–2θ x-ray diffraction patterns of standard YBCO and nanocomposite YBCO+Y2O3 films (not reported here) only show 00l peaks, which confirm the c-axis-oriented epitaxial growth in the films' crystal structure. The relative intensity of the (00l) reflections is nearly constant when Y2O3 species were introduced into the film. However, the length of the caxis of the Y2O3-added samples increases with the Y2O3 content when compared to the c-axis of the standard YBCO reference sample, as listed in table 1.

Table 1. Comparison between the properties of several YBCO films that incorporate APCs.

Sample	c-axis (A)	FWMH Δω (deg)	Tc (K)	ΔTc (K)	Reference
YBCO	11.684	0.22	90.54	3.29	This work
YBCO+Y2O3 2.51A%	11.691	0.227	89.26	4.07	[18]
YBCO+Y2O3 5.44A%	11.697	0.234	89.2	4.96	This work
YBCO+Y2O3 9.22A%	11.719	0.25	87.78	5.69	This work

The full width at half maximum, Δω, of the standard YBCO <005> reflection has broadened by increasing the Y2O3 content. It is apparent that the increment of the Y2O3 species has a direct effect on the small but gradual deterioration of the crystallinity of the YBCO films. These features are similar to those found in the crystal structure of YBCO films with systematically added perovskite compounds such as BaZrO3, BaSnO3, and BaHfO3, which form nanorods inside the films [10–13]. Table 1 also summarizes the behaviors of Tc and ΔTc as a function of Y2O3 content. The resistivity-temperature curves (not shown) have a linear metallic feature, and the onset of the superconducting transition is slightly depressed by introducing Y2O3 as defects. It is worth pointing out that the slight Tc depression is less pronounced in the case of Y2O3 doping than in the case of 1D APC doping. For example, the Tc of the Y2O3 5.44A% sample is 89.2 K, while YBCO+ BaZrO3 4 wt% film had a Tc≈ 87 K [15].

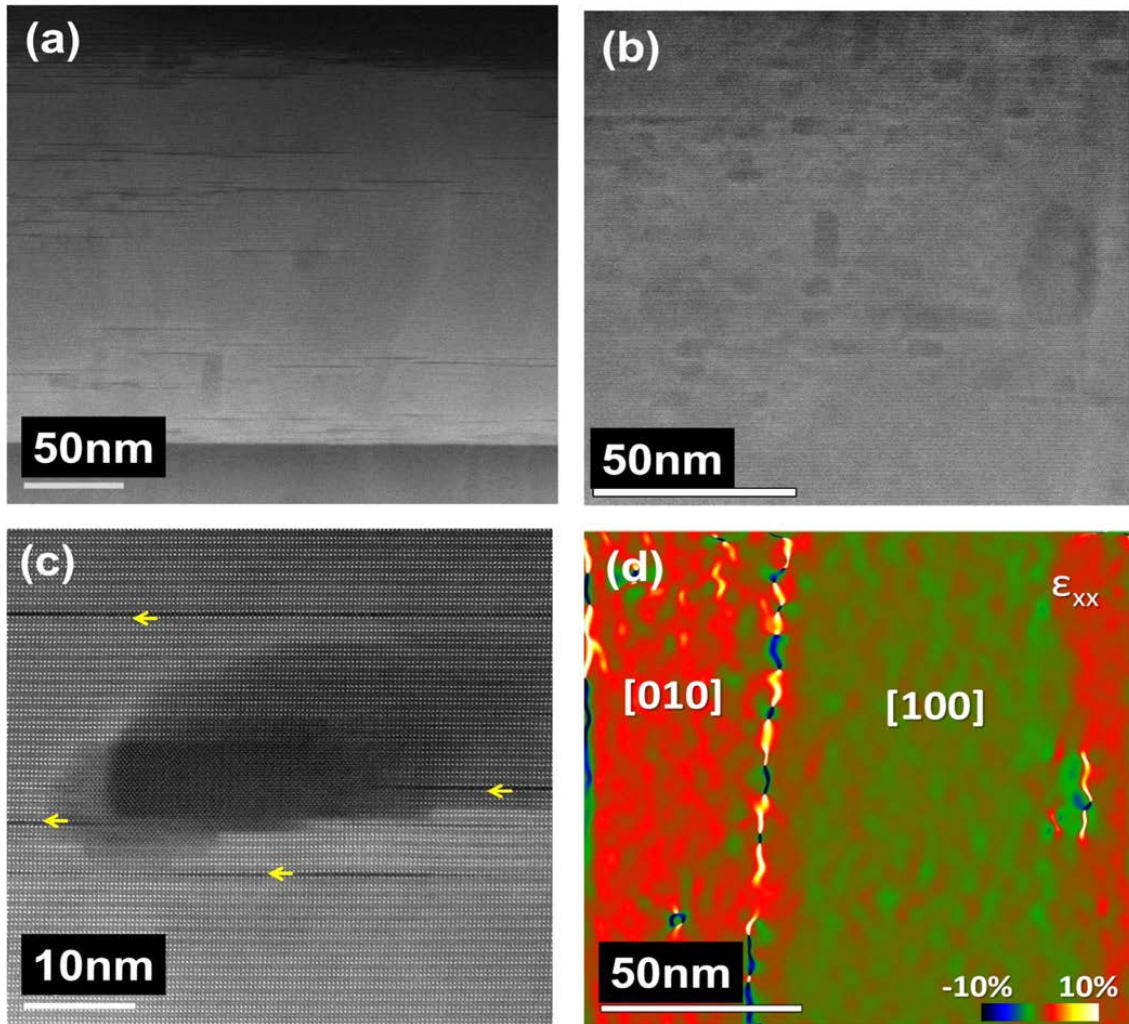Detailed TEM analysis of YBCO + 5.44A% Y2O3 film is shown in figure 1.

Figure 1. Scanning transmission electron microscopy (STEM) analysis of YBCO+ 5.44A% Y_2O_3 thin film. (a) High-magnification crosssectional high-angle annular dark-field scanning transmission electron microscopy (HAADF-STEM) image showing $Y_2Ba_4Cu_8O_{16}$ (Y248) intergrowths as black horizontal lines. (b) Zoom of a region free of Y248 intergrowths, showing the distribution of Y_2O_3 particles of varied dimensionality. (c) High resolution transmission electron microscopy (HRTEM) image of a Y_2O_3 nanoparticle embedded in a superconducting matrix. Arrows indicate Y248 intergrowths. (d) ε_{xx} deformation map, shown in color (red and green). Different deformation values in the whole area of figure 1(b) [010] and [100] zone axes are depicted in red and green, respectively. Bottom region of figure 1(b) was taken as a reference area.

As shown in the low-magnification HAADF-STEM image in figure 1(a), randomly distributed Y2O3 nanoparticles and Y2Ba4Cu8O16 (Y248) intergrowths (dark stripes running parallel to the (001) YBCO plane in the figure) are found within the YBCO matrix. The HAADF detector in a STEM microscope allows the recording of incoherent Z-contrast images. In these images, the intensity of the atom columns directly reflects their mean square atomic number (Z), which helps to unambiguously identify the Y248 intergrowths consisting of an extra Cu-O chain layer. The amount of Y248 can be estimated as 7.74×10^{14} m^{-2} from the STEM image analysis. The

HAADF-STEM image of figure 1(b) shows the morphologies of different Y2O3 nanoparticles. Whereas most of the Y2O3 particles are faceted, some are round, with a few Y2O3 nanorods that are ~20 nm long. By using TEM-energy dispersion spectrometry analysis, we confirmed that the nanoparticles are constituted by Y-rich, Ba- and Cu-poor phases, which is most likely to be Y2O3. The amount of particles per square meter is approximated at 2.68 × 1015 m−2. The amount of Y2O3 nanoparticles is critical in favoring the formation of Y248 intergrowths, which are likely to appear during the film growth process. High-resolution HAADFSTEM images like the one in figure 1(c) show that the epitaxial relationships between YBCO and the Y2O3 nanoparticles is (001)YBCO//(001)Y2O3, and [100]YBCO//[110] Y2O3. Thus, the Y2O3 nanoparticles' a-axis is rotated 45° with respect to the YBCO a-axis, while keeping the same outof- plane orientation, in agreement with x-ray analyses. Therefore, the epitaxial strain of Y2O3 on YBCO may be calculated as −6.85%, less than −8.83% and −7.54%, which can be calculated for BaSnO3 on YBCO and BaZrO3 on YBCO, respectively (cube-on-cube relationship). The lower strain between the YBCO film and the Y2O3 inclusions may be at the origin of the lower suppression of Tc in thesesamples, as compared to other kinds of inclusions. It is remarkable that our YBCO samples with Y2O3 nanoparticles deposited by PLD always present a fixed crystalline orientation, which is at odds with Y2O3 and the perovskite nanoparticles prepared using chemical methods [19, 20, 27], which present random orientation. The STEM images reveal distortions of the YBCO lattice, mostly bending of the YBCO (100) plane, at the interface with the Y2O3 nanoparticles. Misfit dislocations have also been observed along the Y2O3 nanorods. In addition, new insights into the structure of the films can be gathered using geometrical phase analysis (GPA) software on the STEM images. GPA software is based on Fourier analysis of high-resolution lattice imaging by selecting a strong Bragg reflection and performing an inverse Fourier transform [28, 29]. The phase component of the resulting complex image gives information on local displacement and the rotation of atomic planes. In the case of YBCO+ 5.44A% Y2O3 films, we took the {100} Bragg reflections. Accordingly [100], and [010] domains can be unambiguously distinguished by GPA due to the existing differences between a- and b-cell parameters in the YBCO orthorhombic phase. In figure 1(d), the [100] and [010] domains are depicted as green and red, respectively. The lattice spacing in the green region (twin domain) is ~1.5% expanded, compared to the latticed spacing in the red region, which is the reference. Figure 1(d) reports the GPA map for the whole area, as taken from figure 1(b). According to this image, typical, small Y2O3 nanoparticles do not appear to block the twin boundary propagation, while the large Y2O3 nanoparticle (~100 nm) on the right side of the image breaks the vertical coherence of the twin boundary. In this set of samples, the quantity of such large Y2O3 particles is quite small, with roughly one big particle accounting for

every 45 round, smaller particles. Therefore, the obstruction of current transport and the depression of critical current are not likely to occur in this kind of microstructure.

The YBCO+ 9.22A% sample, however, presents a rather different microstructure, as shown in figure 2. The Y248 intergrowths are homogenously distributed and are much extended in length, by several hundreds of nanometers compared to those observed in the YBCO+ 5.44A% Y_2O_3 samples seen in figure 1(a). The concentration of Y248 intergrowths is therefore very high (1.41 × 1016 m−2), with a separation distance of ~5 nm, as observed in the HAADFSTEM image of figure 2(c). Going back to figure 2(b), it clearly shows the presence of a large amount of Y_2O_3 small nanoparticles embedded within the YBCO matrix, coexisting together with the Y248 intergrowths. Interestingly, there is no presence of large Y_2O_3 particles. The amount of Y_2O_3 here is 5.23 × 1015 m−2, higher than in the 5.44A% sample. Since in the 2.51A% Y_2O_3-added YBCO sample [18] 1.75 × 1015 m−2 particles were observed, it is possible to state here that the concentration of particles is proportional to the area of the Y_2O_3 sector attached to the YBCO target. The consequence of the steady increment of Y_2O_3 nanoparticles per sector eventually results in the reduction of pin spacing, d (nm), which is calculated to be 20, 18, and 12 for these samples.
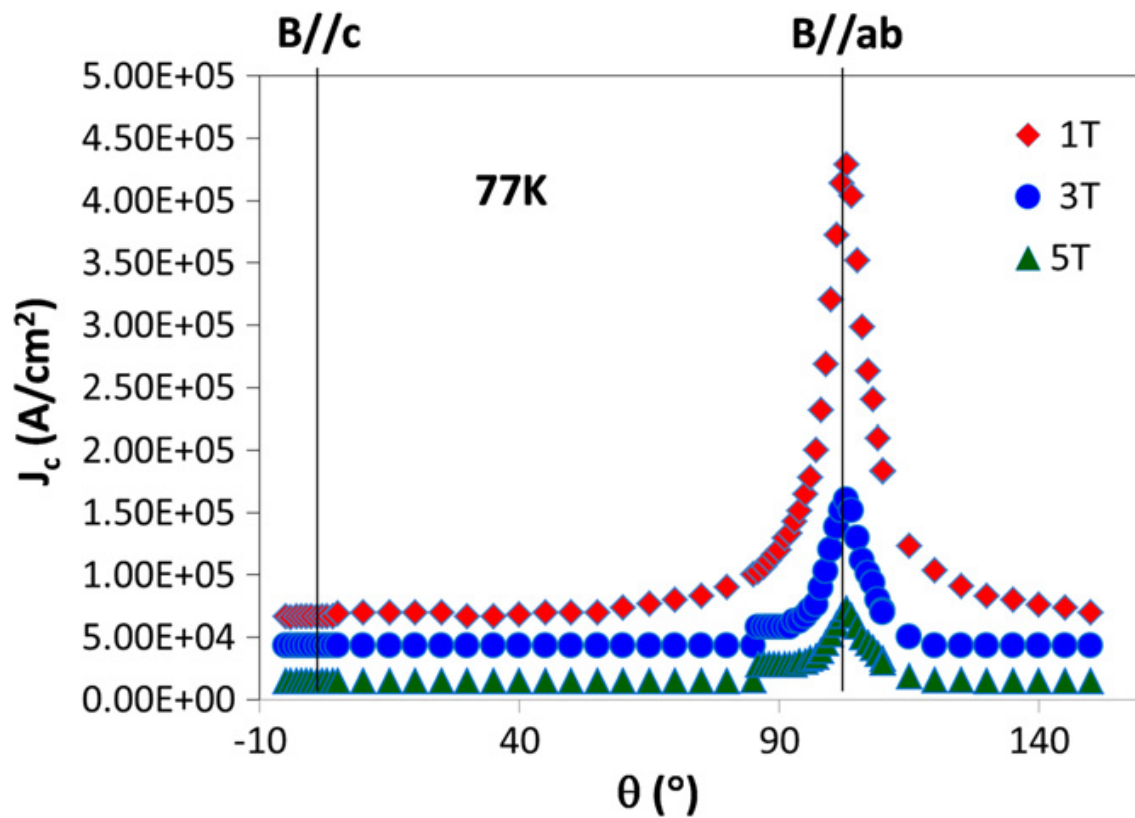

Figure 3. Angular dependence of critical current density (77 K, B = 1, 3, 5 T) for YBCO+Y_2O_3 2.51A%.

Figure 3 shows a representation for the angular dependence, Jc(θ), measured on the 2.51A% Y2O3-added YBCO sample at magnetic fields B/c (77 K) = 1, 3, and 5 T. The absence of the Jc peak for B//c orientation is a clear sign of random pinning due to 3D-type defects that are randomly incorporated inside the YBCO film. Figure 3 represents thegeneral peculiarity of nanoparticle-defects pinning that enhances the Jc of the YBCO samples enriched by thedispersion of Y2O3 or BZO [8, 30, 31], and an iron-based BaFe2As2 superconductor added with BZO [32].
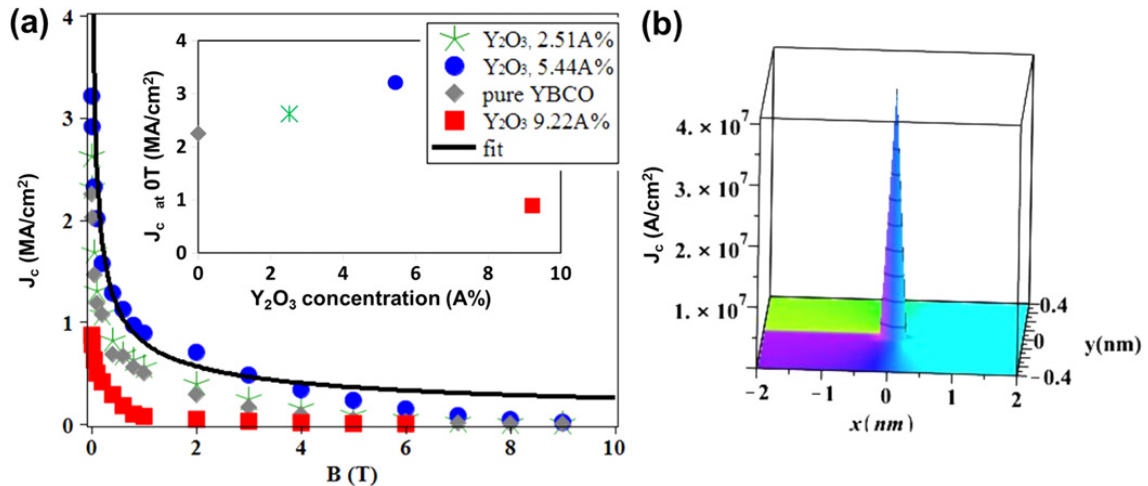

Figure 4. (a) Critical current density, J_c, versus magnetic field, B (77 K, B//c), for a pure YBCO film and doped YBCO films with Y_2O_3nanoparticles. A plot of YBCO+Y_2O_3 2.51A% is taken from [18]. Fit based on single-vortex dynamics is plotted along with experimental data. Inset shows the behavior of J_c(B = 0) in a function of Y_2O_3 concentration. (b) 3D viewing of a single vortex swivelling around the near zero field. Pinning potential in the xy (nm) plane is assumed to be uniform.

Figure 4(a) shows the field dependence, Jc(B), for the standard YBCO, along with YBCO samples added with 2.51A%, 5.44A%, and 9.22A% Y2O3. The inset of figure 4(a) shows the behavior of Jc(B = 0) in a function of Y2O3 concentration. It is clear that Jc(B = 0) is far better when the concentration of Y2O3 nanoparticles in the YBCO film is 5.44A%, suggesting the effectiveness of the introduced pinning centers. However, the enhancement of Jc(B = 0) is less pronounced in the sample with 2.51A% Y2O3. The Jc(B=0) behavior of the 9.22A% Y2O3 concentrated sample is moderately poor compared to the rest of samples, including the standard YBCO shown in the figure. In the case of the heavily doped region of the samples, it is conceivable that superconducting properties such as Tc, Jc, and the upper critical field Bc2 become lower while the superconducting coherence length, ξc, elongates in comparison with the same values of the neighboring undoped superconducting matrix. The pinning strength of this region may be weakened due to the depressed condensation energy associated with superconducting flux lines that are momentarily displaced by the kinetic energy of the Lorentz force. By virtue of proximity, the disappearance of superconductivity in the heavily doped region of the sample

leads to the degradation of superconducting properties in the undoped matrix, and hence, the much lower Jc(B = 0) in the 9.22A% sample.
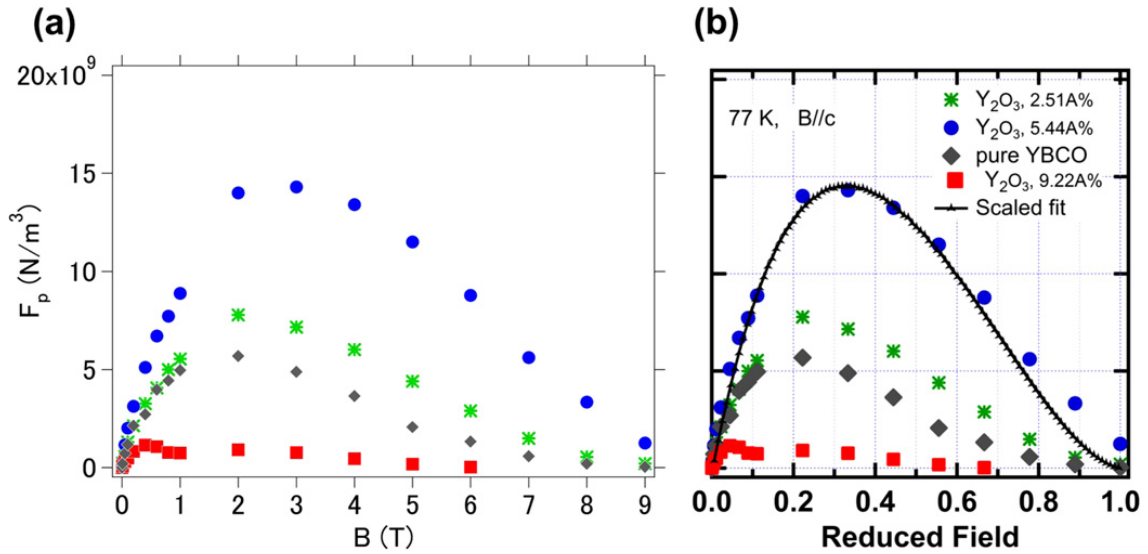

Figure 5. (a) Global pinning forces, F_P, at 77 K as a function of the magnetic field ($F_P = J_c \times B$) applied parallel to the c-axis. Plot of YBCO+Y_2O_3 2.51A% is taken from [18]. (b) Global pinning force, F_P, versus the reduced field $b = B/B_{irr}$ at 77 K and B//c. Theoretical $b = 0.35$ is within 2% of the experimental error. Note that $F_P = 1.3$ GN m^{-3} at $b = 1$.

Figure 5(a) shows the global pinning forces, FP, at 77K as a function of the magnetic field (FP = Jc × B) applied parallel to the c-axis. In both figure 4(a) and figure 5(a), the Jc and FP values of YBCO+ 2.51A% Y2O3 [18], which was prepared following the same experimental procedure, are plotted for comparison. The defects enhance the Jc and FP values of the Y2O3-added samples when compared to the standard YBCO film. The 5.44A% Y2O3 sample produced the global pinning force of 14.3 GN m−3 at 77 K, which is two times the value obtained in the 2.51A% Y2O3 sample, and is comparatively similar to the global pinning of NbTi tape at 4.2 K [33]. Furthermore, the value obtained in YBCO films added with BaZrO3 nanorods was approached with much less depression in the superconducting critical temperature [15].

However, the pinning force is not always proportional to the Y2O3 concentration for the whole series of samples studied. The 9.22A% Y2O3 films present global pinning values lower than the standard YBCO film.

In figure 5(b), the global pinning force data shown in figure 5(a) is depicted as a function of reduced magnetic field b at 77 K. The scaling laws commonly used to approximate the sample's underlying volume pinning force density (f (b)) mechanisms at various fields and temperatures are given by

$$F_P\left(\frac{B}{B_{irr}}\right) \propto \left(\frac{B}{B_{irr}}\right)^m \left(1 - \frac{B}{B_{irr}}\right)^n \text{ or } F_P(b) \propto (b)^m(1 - b)^n$$

where $b = \frac{B}{B_{irr}} \approx \frac{B}{B_{c2}}$ is the reduced field,, B_{irr} is the irreversibility field extracted from the

$J_c(B)$ curves of figure 4 when Jc approaches zero in value, and B is the applied magnetic field. (FP)max is the maximum global pinning force. m = 0.0–1.5, and n = 1.0–2.0 are the pinning parameters. The introduction of Y2O3 nanoparticles to the YBCO sector has an appreciable effect on the volume pinning distribution in all samples compared to the standard YBCO sample. The 9.22A% sample shows (FP)max at considerably low fields before decaying slowly to lower values. This feature is consistent with the moderately poor superconducting performance of this sample due to the presence of an overwhelming nonsuperconducting portion embedded in its superconducting matrix. Sample 2.51A% and the standard YBCO share the same reduced field value of b ≈ 0.23 at their respective maximum pinning positions, whereas sample 2.51A% has a higher global pinning force. Notwithstanding the difference in pinning position across the fields, the global pinning force of both samples shows an identical decreasing feature. However,the flux pinning characteristics of sample 5.44A%, as a function of a magnetic field, are superior throughout the measuring fields at 77 K. Its pinning force smoothly rises to a higher value and reaches a maximum of 14.3 GN m−3, which corresponds to a reduced field of ~0.35. Experimental data of this sample exhibit a good scale, in agreement with the theoretical line prediction for nanoparticles or point pinning.

Nanoparticulate defects such as Y211 and Y2O3 are believed to act as strong pinning centers so that vortices bend into individually pinned segments [3, 34–36]. In this framework, it is possible to estimate the maximum critical current, Jc, from the depinning of curve segments, which are fixed by two consecutive nanoparticles separated by a distance, d,

$$J_c{}^{max} = \frac{\Phi_0}{4\pi\mu_0\lambda_{ab}\lambda_c d}\ln\frac{d}{\xi_c} \quad (1)$$

where Φ0 is the flux quantum, μ0 is the magnetic permeability, λab and λc are the London penetration depths in the ab plane and along the c-axis, respectively, and ξc is the coherence length along the c-axis. If we use the typical values of YBCO parameters at 77 K, (λab = 0.35 μm, λc = 2.4 μm, ξc = 0.6 nm) and the mean separation between Y2O3 particles d~18 nm8, as deduced from TEM images for the Y2O3 5.44A% sample, the estimated Jc (77 K, self-field) is

6.4MA cm−2. The relative consistency with the experimental value of 3.21 MA cm−2 demonstrates that Y2O3 particles act as good pinning centers. Indeed, the effective current blocking is only 13% of Jc.9 Therefore, a percolation path of superconducting current is assured. In the case of the 9.22A% sample, with the mean separation distance between particles ~12 nm, the calculations give Jc (77 K, selffield) = 7.4 MA cm−2, while the experimental value is just 0.89MA cm−2. Based on these analyses, one can visualize that the depression of Jc in the 9.22A% sample may be due to the presence of dense, nonsuperconductive particles that constitute about 32% current blocking. The measured and calculated values of Jc and related parameters are summarized in table 2.

8 Estimated from TEM pictures by image analysis software (ImageJ) as the ratio between the summary of the areas of Y_2O_3 particles and the total area. 9 Spacing, d, is calculated as $d=2/\sqrt{\pi C}$, where C is the areal concentration of Y_2O_3 nanosized inclusions.

Table 2. Summary of measured and calculated values of critical currents and related physical parameters of Y2O3-added YBCO films.

Y_2O_3 content	2.51A%	5.44A%	9.22A%
Amount of APCs (m^{-2})	1.75×10^{15}	2.68×10^{15}	5.23×10^{15}
T_c (K)	89.26	89.2	87.78
d (nm) [37]	20	18	12
Calculated J_c (0T, 77K) (MA/cm^2) with equation (1)	5.93	6.4	7.4
Measured J_c (0T, 77K) (MA/cm^2)	2.62	3.21	0.89
J_c calc./J_c meas.	2.26	1.99	8.31
Effective current blocking [38]	10%	13%	32%

An additional reason for the depression of Jc in the 9.22A% sample is the presence of a considerable amount of Y248 intergrowths. Since the presence of this amount of Y248 intergrowths is indicative of a poorly superconducting material, the intergrowths may also act as good pinning centers if their size is on the same level as the vortices (a few tens of nanometers). However, in the case of this particular sample, Y248 are present in the form of 'disks' situated perpendicular to the c-axis of the film, with a length of several hundreds of nanometers; these disks hinder the current transport.

To account for the thickness-dependent structure in a multiscale YBCO film and its critical current density, the dynamic single-vortex model [3] postulates that the 3D pinning current Jc0 = Jc (d)/(1 − d f ,c/d f) when the film's thickness, d f , is much greater than its critical value, d f ,c. As can be deduced from equation (1), up to 20% of the maximum value of Jc = Jd max , the Ginzburg–Landau depairing current density in YBCO films is experimentally achievable when the pinning separation distance, d, is smaller than λ [3, 35]. For a dynamic single vortex with a dominant pinning force and a uniform pinning potential in the xy plane of the film, the maximum theoretical Jc circulating over the depinned curve segment can reach 40 MA cm−2. For this reason, we used the Bessel function of integer n and its solution in the first quadrant to study the behavior of Jc (B). The method presented in [3] also holds true for the purpose of this study.

In the vicinity of zero field, the maximum depinning Jc (B ≅ 0) behavior of a single vortex can be generated from the large argument forms of the Bessel differential equation:

$$x^2 y'' + xy' + (x^2 - v^2)y = 0$$

One of the solutions to the Bessel equation that can be applied to calculate the internal current distribution within a cylindrical conductor is:

$$I_n(x) = \sum_{\kappa=0}^{\infty} \frac{(-1)^{\kappa}}{\kappa!\, \Gamma(\kappa + v + 1)} \left(\frac{x}{2}\right)^{2\kappa + v} \qquad (2)$$

where In is the Bessel function of integer order n=0, 1, 2,...,x is any positive quantity corresponding to Cλ Jc/ξuJd 2 or d/πλ as in [3], v = 0.5, κ = 0, 1, 2,..., and

$$\Gamma(\kappa + v + 1) = \frac{(2\kappa + 1)!}{2^{2\kappa+1}\,\kappa!} \sqrt{\pi}$$

The asymptotic behavior of equation (2) yields the following expression for depinning Jc (B) for a vortex line strongly pinned to the film's surface by the presence of defects,

$$J_c(B) = \sqrt{\frac{2}{\pi x}} \cos \phi$$

Where

$$\phi = \left[\pi B - \left(n.\frac{\pi}{2} \right) - \frac{\pi}{4} \right] \approx 0.007°$$

is the angle of critical bending. Henceforth, to satisfy the depinning condition for the vortex critical bending, we use these expressions to generate a 3D plot for the single-vortex dynamics in a superconductor with a 3D pinning size and its effect on the critical current density for the samples studied. Indeed, the minimum vortex core length that can be pinned is obtained by dividing the experimental Jc (B = 0) value obtained from each of the samples over the maximum calculated current of 40 MA cm−3.

A fit based on equations (2) and (3) is depicted in figure 4(a), along with experimental data. In comparison with the standard YBCO film, the 5.44A% Y2O3 sample shows a good field-dependent Jc up to 4 T. This result suggests that sample 5.44A% Y2O3 has a relatively denser array of small, strong pins as compared to other samples, which is obviously the case considering, among others, the previously detailed morphological analysis. Beyond 4 T, however, the Jc of all samples decreases below the curve of the depinning current density. As shown in figure 4(b), the maximum attainable Jc for YBCO films is 40 MA cm−2. This value corresponds to the maximum current density through the normal direction of a vortex core swiveling around the vicinity of magnetic field B≈0 T [3]. For YBCO samples added with 2.51A%, 5.44A%, and 9.22A% Y2O3, the minimum vortex core length that can be pinned by the flow of a supercurrent is estimated to be about 6.5%, 8.0%, and 2.2%, respectively. As the lowfield regime is known to characterize the single-vortex dynamics, the Jc(B) of the 5.44A% Y2O3 sample is seen to have quite good consistency with the positive effect of Y2O3 nanoparticles.

4. Conclusion

The evolution of the morphology of Y2O3-added YBCO films prepared by surface-modified target technology demonstrates that it is not easy to control the size and also separate the Y2O3 nanoparticulate inside the YBCO films. However, the particles are not randomly oriented, but present in good epitaxial relationship with the YBCO. As can be expected, the total amount of Y2O3 nanoparticles dispersed in YBCO films increases with the area of the Y2O3 sector that is attached to   the standard YBCO target. The 5.44A% Y2O3-added sample presented a maximum value of global pinning force (14.3 GN m−3 at 77 K) in this series of samples, approaching the value obtained in YBCO films with added BaZrO3 nanorods, albeit with a lesser depression in the superconducting critical temperature. This is attributed to good compromise between the moderate concentration of Y2O3 particles (2.68 × 1015 m−2) and a relatively low amount of Y2Ba4Cu8O16 (Y248) intergrowths, which have a sizable presence of 7.74 × 1015 m−2, leading to the effective pinning of vortices without significant current hindrance. At the lowfield regime, the amount of Y2O3 5.44A% nanoparticles incorporated into this sample was found to generate 8.0% effective pinning along the vortex core length. The singlevortex dynamics model fits well with the data of the YBCO+Y2O3 5.44A% sample in the low-field span up to 4 T.

References

[1] Larbalestier D C, Gurevich A, Feldmann D M and Polyanskii A 2001 Nature 414 368

[2] Paranthaman M and Izumi T 2004 Mater. Res. Soc. Bull. 29 533

[3] Gurevich A 2007 Supercond. Sci. Technol. 20 S128

[4] Foltyn S R, Civale L, MacManus Driscoll J L, Jia Q X, Maiorov B, Wang H and Maley M 2007 Nat. Mater. 6 631

[5] Matsumoto K and Mele P 2010 Supercond. Sci. Technol. 23014001

[6] Obradors X, Puig T, Palau A, Pomar A, Sandiumenge F, Mele P and Matsumoto K 2011 Nanostructured superconductors with efficient vortex pinning ed D L Andrews, G D Scholes and G P Wiederrecht Comprehensive Nanoscience and Technology vol 3 (Oxford: Academic Press) pp 303–49

[7] Mele P, Matsumoto K, Horide T, Miura O, Ichinose A,Mukaida M, Yoshida Y and Horii S 2006 Supercond. Sci. Technol. 19 44

[8] MacManus Driscoll J L, Foltyn S R, Jia Q X, Wang H, Serquis A, Civale L, Maiorov B, Hawley M E, Maley M P and Peterson D E 2004 Nat. Mater. 3 439

[9] Goyal A et al 2005 Supercond. Sci. Tech. 18 1533

[10] Ichinose A, Naoe K, Horide T, Matsumoto K, Kita R, Mukaida M, Yoshida Y and Horii S 2007 Supercond. Sci. Tech. 20 1144

[11] Yamada Y et al 2005 Appl. Phys. Lett. 87 132502

[12] Mele P, Matsumoto K, Horide T, Ichinose A, Yoshida Y, Mukaida M, Horii S and Kita R 2008 Supercond. Sci. Technol. 21 032002

[13] Shiohara Y, Yoshizumi M, Takagi Y and Izumi T 2013 Physica C 484 1

[14] Varanasi C V, Barnes P N, Burke J, Brunke L, Maartense I, Haugan T J, Stinzianni E A, Dunn K A and Haldar P 2006 Supercond. Sci. Tech. 19 L37

[15] Mele P, Matsumoto K, Horide T, Ichinose A, Mukaida M, Yoshida Y and Horii S 2007 Supercond. Sci. Tech. 20 244

[16] Haugan T, Barnes P N, Wheeler R, Meisenkothen F and Sumption M 2004 Nature 430 867

[17] Gapud A A, Kumar D, Viswanathan S K, Cantoni C, Varela M, Abiade J, Pennycook S J and Christen D K 2005 Supercond. Sci. Tech. 18 1502

[18] Mele P, Matsumoto K, Horide T, Ichinose A, Mukaida M, Yoshida Y and Horii S 2007 Supercond. Sci. Technol. 20 616

[19] Gutierrez J et al 2007 Nat. Mater. 6 367

[20] Llordes A et al 2012 Nat. Mater. 11 329

[21] Miura M, Kato T, Yoshizumi M, Yamada Y, Izumi T, Shiohara Y and Hirayama T 2008 Appl. Phys. Express 1051701

[22] Solovyov V F, Wiesmann H J, Wu L, Li Q, Cooley L D, Suenaga M, Maiorov B and Civale L 2007 Supercond. Sci. Technol. 20 L20

[23] Chen Z, Feldmann D M, Song X, Kim S I, Gurevich A, Reeves J L, Xie Y Y, Selvamanickam V and Larbalestier D C 2007 Supercond. Sci. Technol. 20 S205

[24] Sparing M, Backen E, Freudenberg T, Huhne R,Rellinghaus B, Schultz L and Holzapfel B 2007 Supercond. Sci. Technol. 20 S239

[25] Maiorov B, Wang H, Foltyn S R, Li Y, DePaula R, Stan L, Arendt P N and Civale L 2006 Supercond. Sci. Technol. 19 891

[26] Mele P, Matsumoto K, Horide T, Ichinose A, Mukaida M, Yoshida Y and Horii S 2007 IEEE Trans. Appl. Supercond. 17 3713

[27] Gazquez J, Coll M, Roma N, Sandiumenge F, Puig T and Obradors X 2012 Supercond. Sci. Technol. 25 065009

[28] Hytch M J, Snoeck E and Kilaas R 1998 Ultramicroscopy 74 131

[29] Guzman R, Gazquez J, Ruoco V, Palau A, Magen C, Varela M, Arbiol J, Obradors X and Puig T 2013 Appl. Phys. Lett. 102 081906

[30] Maiorov B, Baily S A, Zhou H, Ugurlu O, Kennison J A, Dowden P C, Holesinger T G, Foltyn S R and Civale L 2009 Nat. Mater. 8 398

[31] Wang H, Serquis A, Maiorov B, Civale L, Jia Q X, Arendt P N, Foltyn S R, MacManus Driscoll J L and Zhang X 2006 J. Appl. Phys. 100 053904

[32] Miura M, Maiorov B, Kato T, Shimode T, Wada K, Adachi S and Tanabe K 2013 Nat. Comms. 4 2499

[33] Meingast C and Larbalestier D C 1989 J. Appl. Phys. 66 5971

[34] Brandt E H 1992 Phys. Rev. Lett. 69 1105

[35] Koshelev A E and Kolton A B 2011 Phys. Rev. B 84 104528

[36] Foltyn S R, Wang H, Civale L, Jia Q X, Arendt P N, Maiorov B, Li Y, Maley M P and MacManus-Driscoll J L l 2005 Appl. Phys. Lett. 87 162505